Direct liquid injection chemical vapor deposition of ZrO2 films from a heteroleptic Zr precursor: interplay between film characteristics and corrosion protection of stainless steel

Sebastian M J Beer, Diane Samelor, Alsayed Abdel Aal, Johannes Etzkorn, Detlef Rogalla, Asiya E Turgambaeva, Jerome Esvan, Aleksander Kostka, Constantin Vahlas, Anjana Devi

Available online at www.sciencedirect.com

jmr&t Journal of Materials Research and Technology

journal homepage: www.elsevier.com/locate/jmrt

Original Article

Direct liquid injection chemical vapor deposition of ZrO_2 films from a heteroleptic Zr precursor: interplay between film characteristics and corrosion protection of stainless steel

Sebastian M.J. Beer [a], *Diane Samelor* [b], *Alsayed Abdel Aal* [c], *Johannes Etzkorn* [c], *Detlef Rogalla* [d], *Asiya E. Turgambaeva* [e], *Jerome Esvan* [b], *Aleksander Kostka* [f], *Constantin Vahlas* [b,**], *Anjana Devi* [a,*]

[a] *Inorganic Materials Chemistry, Ruhr University Bochum, Universitätsstr. 150, 44801 Bochum, Germany*
[b] *CIRIMAT – CNRS, Université de Toulouse, 4, Allée Emile Monso, BP-44362, 31030 Toulouse Cedex 4, France*
[c] *Chemistry and Materials Engineering, Fachhochschule Dortmund, Sonnenstr. 96-100, 44139 Dortmund, Germany*
[d] *RUBION, Ruhr University Bochum, Universitätsstr. 150, 44801 Bochum, Germany*
[e] *Nikolaev Institute of Inorganic Chemistry SB RAS Pr. Lavrentiev 3, Novosibirsk 630090, Russia*
[f] *Center for Interface Dominated Materials (ZGH), Ruhr University Bochum, Universitätsstr. 150, 44801 Bochum, Germany*

ARTICLE INFO

Article history:
Received 24 January 2021
Accepted 24 May 2021
Available online 29 May 2021

Keywords:
Chemical vapor deposition
Zirconium oxide
Corrosion protection
Thin film analysis
Electrochemical impedance spectroscopy

ABSTRACT

The direct liquid injection chemical vapor deposition (DLI-CVD) of uniform and dense zirconium oxide (ZrO_2) thin films applicable as corrosion protection coatings (CPCs) is reported. We present the entire development chain from the rational choice and thermal evaluation of the suitable heteroleptic precursor $[Zr(O^iPr)_2(tbaoac)_2]$ over the detailed DLI-CVD process design and finally benchmarking the CPC behavior using electrochemical impedance spectroscopy (EIS). For a thorough development of the growth process, the deposition temperature (T_{dep}) is varied in the range of 400 – 700 °C on Si(100) and stainless steel (AISI 304) substrates. Resulting thin films are thoroughly analyzed in terms of structure, composition, and morphology. Grazing incidence X-ray diffractometry (GIXRD) reveals an onset of crystallization at $T_{dep} \geq 500$ °C yielding monoclinic and even cubic phase at low temperatures. At $T_{dep} = 400$ °C, isotropic growth of XRD amorphous material is shown to feature cubic crystalline domains at the interfacial region as revealed by electron diffraction. Corrosion results obtained through EIS measurements and further immersion tests revealed improved CPC characteristic for the 400 °C processed ZrO_2 coatings compared to the ones deposited at $T_{dep} \geq 500$ °C, yielding valuable insights into

* Corresponding author.
** Corresponding author.
E-mail addresses: constantin.vahlas@toulouse-inp.fr (C. Vahlas), anjana.devi@rub.de (A. Devi).
https://doi.org/10.1016/j.jmrt.2021.05.068

the correlation between growth parameter and CPC performance which are of high relevance for future exploration of CPCs.

1. Introduction

Over the last decades, zirconium(IV) dioxide (zirconia, ZrO_2) thin films have attracted considerable attention from research and industry owing to their outstanding chemical and physical properties, enabling applications in microelectronics [1,2], optics [3], catalysis [4–6], chemical sensors [7] and as protective coatings. Especially for the latter, properties such as a high thermal robustness, mechanical strength, low thermal conductivity, and high erosion resistance are optimal for the use as thermal barrier coatings (TBCs) [8–12]. Moreover, the thermal expansion coefficient of ZrO_2 is close to that of many metals, thus preventing thermally induced stress and cracks during formation and operations [13]. This, in combination with a superior chemical inertness against extreme pH and oxidation environments makes ZrO_2 films an ideal candidate for the protection of metal surfaces as corrosion protection coating (CPC) [14–18]. Indeed, Li et al. [16] demonstrated a 6.5 times higher oxidation resistance of ZrO_2 coated steel compared to uncoated ones. Also, Yu et al. [18] reported an enhanced corrosion resistance of ZrO_2 films coated stainless steel (AISI 304) in coal-gas environment, even during exposure in H_2S gas at temperatures above 600 °C.

For corrosion protection, cubic ZrO_2 is favored over the other two known, monoclinic, and tetragonal polymorphic forms, based on the promising properties such as high density. However, the stabilization of the cubic phase requires higher temperatures or, alternatively, doping with MgO or Y_2O_3. More recently, the approach to fabricate multicomponent systems such as of CeO_2/ZrO_2 [19] or ZrN/ZrO_2 [20] yielded an improvement for the passivation of stainless steel surfaces.

Hitherto, a multitude of different physical vapor deposition (PVD) techniques for the deposition of such CPC ZrO_2 thin films have been successfully established, featuring pulsed laser deposition (PLD) [21], magnetron sputtering [22] or ion plating [20]. Despite their line-of-sight deposition mode, elaborated kinematic modes of the parts to be treated with regard to the ion sources allow growing highly structured ceramics of several micrometers on complex structured substrate geometries with high deposition rates [23–27]. However, such processes cannot treat all types of complex-in-shape parts and they may exhibit microscopic imperfections like pinholes due to growth defects [28], lowering the corrosion protection characteristics of thin films [29].

Solution-based chemical processes such as sol–gel [18,30–32] or spin-coating [17] have been extensively studied based on the simple and low-cost fabrication of the coatings. Still, unsatisfactory thin film homogeneity, structure-control and especially crack formation as a consequence of the large volume shrinkage during the film formation [33] degrade the anticorrosion performance and remain problematic.

Chemical vapor deposition (CVD) serves as a promising alternative coating method to the above-mentioned techniques. It allows a structure-controllable conformal film growth over large and complex substrate geometries. Despite its potential, the number of publications investigating the CVD growth of ZrO_2 on stainless steel and metal substrates in general is rather limited in terms of CPCs [34,35]. Most of the research investigates the growth of ZrO_2 or yttria stabilized zirconia (YSZ) for application as TBC as highlighted in the review by Garcia and Goto [8].

This might be attributable to the specific demands and requirements for TBCs such as significantly thick and porous films, whereas CPCs on metal substrates are thin, dense, and pinhole-free. Notably, some stainless steels are prone to oxidation at elevated temperatures, thus requiring a careful process development considering moderate deposition temperature, precise structural growth, or a tunable deposition rate. Appropriately tuned CVD processes can circumvent the above-mentioned limitations, particularly by monitoring the deposition chemistry.

In the ideal case, the application of CVD processes for the fabrication of CPCs could significantly enhance the durability of steel parts for industrial applications, especially regarding the steel molds for plastic industry. Indeed, CVD of uniform and conformal barrier coatings applied on complex tool shapes are expected to ensure a high quality of the product surface without sacrificing tool dimensions and subsequently fulfilling high quality standards.

In this perspective, the design of both, suitable compounds as CVD precursors, and technological solutions to introduce the source gas in the deposition chamber, play a pivotal role in the optimization of the CVD process.

Oxygen-coordinated compounds have been found to serve as a versatile precursor family for the deposition of ZrO_2 films. This is based on their pre-existing Zr–O bond and the absence of further heteroatoms such as halogens, phosphorous or nitrogen, which could lead to contamination in the films. One of the most commonly used precursors, $[Zr(O^tBu)_4]$ (O^tBu = *tert*-butoxide) provides a high reactivity towards co-reactants, but possesses a poor thermal stability and shelf life, undergoing catalytic hydrolytic decomposition, when exposed to slight traces of water or ambient, thus making it difficult to handle [36]. To overcome these drawbacks, $[Zr(thd)_4]$ (thd = 2,2,6,6 tetramethylheptadienato) was studied extensively as CVD precursor. Based on the spatial shielding and saturation of the Zr^{4+} metal center by the thd ligand, the elimination of dimerization effects was obtained, but only at the expense of a lower volatility and reactivity [37].

Alternatively, the heteroleptic bis(isopropoxide)bis(*tert*-butylacetoacetate) zirconium (IV) $[Zr(O^iPr)_2(tbaoac)_2]$ combines the beneficial characteristics of the alkoxy groups with the acetoacetate ligand forming a highly versatile precursor. The alkoxide (O^iPr) functions increase the reactivity due to the

unsaturated coordination sphere of the Zr^{4+} metal center whereas the bidentate (tbaoac) groups contribute to an increased thermal stability of the compound while maintaining a high solubility due to the etheric side chain making it an attractive precursor for solvent-assisted processes. Furthermore, the introduction of the cleavage point of the ester function in the β-ketoester ligand enables lower precursor decomposition temperatures compared to the conventional bidenate β-diketonates [38,39]. Additionally, $[Zr(O^iPr)_2(tbaoac)_2]$ features a straightforward and simple synthesis with good yields and can be scaled-up easily, which renders this compound as a promising candidate for the deposition of ZrO_2. This heteroleptic precursor design concept was successfully tested using $[Zr(O^iPr)_2(tbaoac)_2]$ and analogues such as $[Zr(O^tBu)_2(mmp)_2]$ (mmp = 1-methoxy-2-methy-2-propanolate) or $[Zr(O^tBu)_2(dbml)_2]$ (dbml = di-*tert*-butylmalonato) in CVD processes for the fabrication of high-k dielectric thin films [38–41].

Compared to the sublimation through conventional heating of the solid precursor, direct liquid injection CVD (DLI-CVD) systems flash-evaporate a solution of well-defined precursor solution in organic solvent, thus loading the precursor molecule with less thermal stress that could lead to its premature decomposition and subsequently to potential clogging of tubes and uncontrollable operation of the deposition process. This, in combination with the excellent reproducibility of experiments, the long-term storability and scalability of these precursor solution, favor DLI-CVD over conventional delivery systems for industrial-scale processes.

Herein, we report the evaluation of the $[Zr(O^iPr)_2(tbaoac)_2]$ precursor with respect to its gas phase stability. We implement it in a newly-developed DLI-CVD process and investigate the growth characteristics of the films deposited on Si(100) and AISI 304 stainless steel substrates at varied deposition temperatures. A detailed characterization of their structure was performed using grazing-incidence X-ray diffraction (GIXRD), selective-area electron diffraction (SAED) and transmission electron microscopy (TEM). The composition of the films was determined using complementary techniques such as X-ray photoelectron spectroscopy (XPS), Rutherford-backscattering spectrometry (RBS), nuclear reaction analysis (NRA), and Fourier-transform infrared spectroscopy (FT-IR). For the analysis of the topography and morphology, atomic force microscopy (AFM) and scanning electron microscopy (SEM) were carried out. Furthermore, the corrosion protection performance of ZrO_2 coatings on AISI 304 were investigated using electrochemical impedance spectroscopy (EIS). These findings are correlated with the results of the films analysis to get insights on the origin of the difference in CPC performance, which allows to benchmark the films for a potential future application on steel tools in industry.

2. Methods

2.1. Precursor synthesis and analysis

The zirconium bis(isopropoxide)bis(*tert*-butylacetoacetate) precursor $[Zr(O^iPr)_2(tbaoac)_2]$ was synthesized according to a literature-known procedure [42] using $[Zr(O^iPr)_4(HO^iPr)]$ (99.9 %, Sigma Aldrich) and *tert*-butylacetoacetate (99 %, Acros). Technical grade n-hexane was dried in an solvent purification system (MBraun) and stored over molecular sieves (4 Å) prior to use. The compound purity was verified by ^{1}H nuclear magnetic resonance (^{1}H-NMR, shown in the Supporting Information Fig. SI 1).

Thermogravimetric analysis and differential scanning calorimetry (TG/DSC) were performed using a Netzsch STA 409 PC LUXX device operated in an argon-filled glovebox at atmospheric pressure. Approximately 20 mg of precursor filled into Al_2O_3 crucible was heated from 35 to 400 °C with a heating rate of 5 K·min^{-1}. Vapor pressure curves were estimated by the method established by Kunte et al. [43] using isothermal thermogravimetric data.

Gas phase compositional analysis of the evaporated precursor in the presence of oxygen was measured through imitation of a miniature CVD equipment consisting of a precursor evaporator connected to a temperature-controllable reactor tube functioning as the deposition chamber. Through an effuse orifice of 0.2 mm diameter, the existing gas mixture was ionized (70 eV) and then detected in a time-of-flight mass spectrometer (TOF-MS). The time for an evaporated molecule to cross the orifice to the MS analyzer did not exceed 1 ms, allowing an in-situ observation of gaseous decomposition products as a function of reactor wall temperature. For the measurement, approximately 2 mg of precursor was heated to 190 °C in a dynamic vacuum with an oxygen partial pressure of 0.5 Pa. The reactor tube was heated from 200 to 400 °C with a ramp rate of 5 K·min^{-1} and the full range mass spectra were recorded every 10 °C during heating.

2.2. Deposition conditions

DLI-CVD of ZrO_2: Deposition of ZrO_2 films was performed in a custom-built, horizontal hot-wall CVD reactor connected to a DLI system (Kemstream). A quartz glass tube (30 cm length and Ø = 2.6 cm) reactor with a stainless steel substrate holder was heated indirectly using a transparent tube furnace. Depositions were made on (1.3 × 1.3) cm^2 Si(100) and (1.5 × 2.0) cm^2 stainless steel AISI 304 (V2A 3D/2R bright annealed, ISO 9445-2, Anton Lippert GmbH) substrates in the temperature range 400 − 700 °C. They were cleaned in an ultrasonic bath with acetone and ethanol before rinsing with HPLC water and drying under argon flow. N_2 (99.9999 %, Messer) flowing at 400 sccm (standard cubic centimeters per minute) was used as dilution gas and the same flow was used as carrier gas for the mixing chamber whereas 100 sccm O_2 (99.9999 % Messer) was fed as reactive gas. Mass flow controllers were used for the regulation of the gas flows. A 0.01 M precursor solution of $[Zr(O^iPr)_2(tbaoac)_2]$ in anhydrous n-heptane (99 %, Alfa Aesar) was used for the DLI. The solution was pulsed into the vaporizer unit with a frequency of 2 Hz and 3 ms valve opening, resulting in gas flows of the precursor and solvent in the deposition zone equal to 13 and 91 sccm, respectively. The heating chamber for the flash evaporation of the precursor aerosol was set to 200 °C. The reactor pressure was adjusted to 10 Torr.

2.3. Thin film characterization

GIXRD at $\omega = 1°$ beam angle was performed in a Bruker D8 Advance instruments equipped with a Cu K_α (1.5418 Å) source and operated at 40 kV/40 mA, Ni filter and Lynxeye detector.

FT-IR spectroscopy measurements of the ZrO_2 films on AISI 304 were recorded with a Thermo Scientific Nicolet iS50 FT-IR spectrometer and a Specac Quest ATR unit (diamond crystal) in the range of 500 – 3500 cm^{-1}.

RBS measurements were performed using a He^+ ion beam with an energy of 2.0 MeV for the detection and quantification of Zr. For the low atomic mass atoms (O, C, N) nuclear reaction analysis (NRA) was carried out using a deuteron ion beam of 1.0 MeV. The SIMNRA program suite was used for the processing of the RBS/NRA raw data [44]. For the analysis of the O composition, an oxidized top layer of the AISI 304 surface was modelled allowing a proper fit between the RBS Zr signal and the NRA data resulting in potential errors, approximately ±10 at.% for O, and ±3 at.% for C and N. A detailed description of the fitting method of RBS on AISI 304 is given in the Supporting Information together with representative examples of the RBS spectra at 400 and 500 °C, shown in Fig. SI 3. The obtained information on the composition of the films was also used to estimate their thickness.

Reflective ellipsometry of ZrO_2 films on Si(100) substrates was performed using a Semilab SE 2000 ellipsometer operated in the range of 250 – 1000 nm wavelength at a 70° incidence angle. A 3 × 3 spot pattern was probed with 2 mm distance between the spots. Data was fitted using the Semilab SEA software using the effective medium approximation (EMA) model to estimate the film thickness.

XPS data was measured using a monochromatized Al K_α source (1486.6 eV) on a ThermoScientific K-Alpha system. The X-ray spot size was adjusted to approximately 400 μm in diameter. The pass energy was fixed at 30 eV with a step of 0.1 eV for core levels and 150 eV for surveys (step 1 V). The spectrometer energy calibration was done using the Au $4f^{7/2}$ (83.9 ± 0.1 eV) and Cu $2p^{3/2}$ (932.8 eV ± 0.1 eV) photoelectron lines. XPS spectra were recorded in direct mode N(Ec) and the background signal was removed using the Shirley method [45]. The flood gun was used to neutralize charge effects on the top surface. An Ar^+ ion beam (500 eV) was used for sputtering the samples (30 and 430 s).

SEM analysis was performed using a JEOL JSM-7200F field-emission scanning electron microscope. The top view images were recorded using a 20 kV acceleration voltage.

AFM was used to study the topography of the ZrO_2 thin films on AISI 304 with a Bruker Dimension device equipped with a "Fastscan" scanner in the "Scanasyst" mode.

TEM measurements on cross-sections of 400 and 500 °C ZrO_2 films on AISI 304 were prepared using a dual-beam FEI Helios G4 CX focused ion beam (FIB) instrument with an acceleration voltage of 30 kV. TEM imaging and selective area electron diffraction (SAED) were performed using a FEI Tecnai F20 instrument operated at 200 kV.

EIS measurements were carried out for the ZrO_2 films deposited on AISI 304 deposited in a range of 400 – 700 °C using an Autolab PGSTAT204 (Metrohm) galvanostat/potentiostat system supported by "Nova 2.1.4" software. A three-electrode setup was realized with a secondary calomel electrode as the reference electrode and a platinum electrode as the counter electrode. The surface area of 95 mm^2 was exposed to the electrolyte of 0.1 wt.% NaCl at (40 ± 0.1) °C.

Prior to each EIS measurement, the open circuit potential (OCP) was recorded for 120 s and the measurements were performed at 0 V vs. OCP with a perturbation amplitude of 10 mV. A single sine mode was employed over a frequency range of 0.1 – 10^4 Hz with ten frequencies per decade to ensure higher accuracy measurements. Under the same conditions, the variation of EIS measurements with different immersion times (30 – 120 min), was investigated for the amorphous and crystalline coatings deposited at 400 and at 500 °C, respectively.

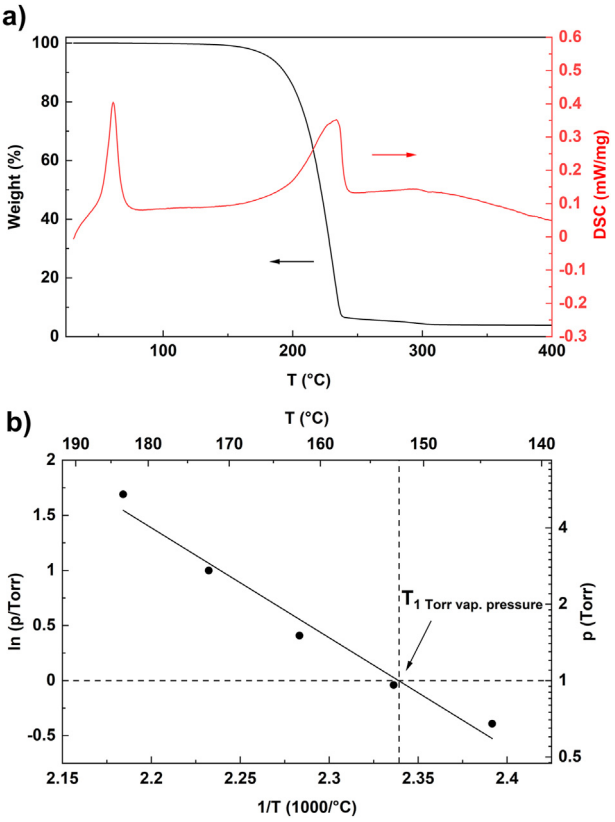

Fig. 1 – a) TG (black) and DSC (red) (TG/DSC) of $[Zr(O^iPr)_2(tbaoac)_2]$. b) Vapor pressure temperature functions of $[Zr(O^iPr)_2(tbaoac)_2]$. In the vapor pressure graph, the evaporation is described as a linear fit (black) with $\ln(p) = -9979.88 \cdot T^{-1} + 23.34297$. The grey lines indicate the 1 Torr vapor pressure temperature of the compound (154.4 °C) to guide the eye.

3. Results and discussion

3.1. $[Zr(O^iPr)_2(tbaoac)_2]$ precursor analysis

3.1.1. Physicochemical properties

As the physicochemical properties of a precursor are known to have a significant impact on chemical vapor deposition

(CVD) process development, a rational choice of the precursor is needed to enable and fine-tune the growth characteristics, especially for corrosion protection coating (CPC) applications in terms of growth temperature, morphology, and composition. $[Zr(O^iPr)_2(tbaoac)_2]$ is known to possess the required physicochemical characteristics for the growth of ZrO_2 thin films [42]. Although this precursor is known from the literature for the growth of dielectric oxides [39], in this study the stability and volatility of the compound was thoroughly investigated by means TG/DSC as well as vapor pressure measurements under inert gas conditions, depicted in Fig. 1.

From the TG curve it is visible that $[Zr(O^iPr)_2(tbaoac)_2]$ evaporates in two distinguishable steps. A first step was determined featuring an onset of evaporation temperature at 203 °C accompanied by a mass loss of 93.5 %. In contrast to that, the second step only exhibits a minor mass loss (~2.6 %) indicating the formation of non-volatile species evaporating until 300 °C. The presence of the rest mass (~3.9 %) leads to the assumption that a partial decomposition takes places at higher temperatures. However, from the curvature of the DSC graph no notable sharp exothermic peaks were observed. Thus, a clean evaporation and thermal stability of the precursor can be expected in the applicable temperature range. From the DSC curve, the melting point of the Zr precursor was graphically estimated to be 52.5 °C.

For a thorough overview of the thermal properties, the 1 Torr vapor pressure temperature ($T_{1\ Torr\ v.p.}$) of the heteroleptic Zr precursor was estimated. The $T_{1\ Torr\ v.p.}$ serves as a figure of merit and allows a benchmark and comparison between different precursor systems. For this, the temperature dependence of the vapor pressure expressed by the Clausius Clapeyron Equation shown in Equation (1) can be used to calculate $T_{1\ Torr\ v.p.}$.

$$\ln(p) = -9979.88 \cdot T^{-1} + 23.34297 \quad (1)$$

with pressure p (Torr) and temperature T (K). The vapor pressure determination using TG measurements was established by Price [46]. From this, a $T_{1\ Torr\ v.p.}$ of 154.4 °C and volatilization enthalpy of 83.0 kJ/mol were estimated. In comparison, $[Zr(thd)_4]$ exhibits a $T_{1\ Torr\ v.p.}$ of around 300 °C (extrapolation) [37] demonstrating the increased volatility of the heteroleptic precursor.

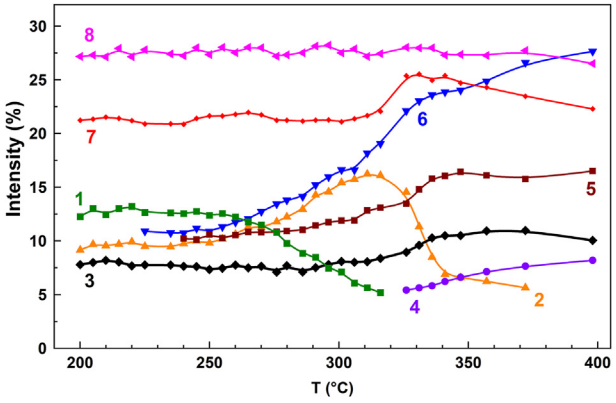

Fig. 2 – Temperature-dependent mass-spectrometric analysis of gas phase composition during the heating of $[Zr(O^iPr)_2(tbaoac)_2]$ in O_2 presence. The detected fragments numbered from 1 to 7 are assigned as follows: (L = tbaoac): 1- $[Zr(O^iPr)L_2\text{-}CH_3]^+$, 2- $[O^iPr]^+$, 3- $[C_4H_8]^+$, $[C_3H_4O]^+$, 4- $[H_2O]^+$, 5- $[C_2H_4]^+$, $[CO]^+$, 6- $[C_3H_8]^+$ or $[CO_2]^+$, 7 $[C_3H_7]^+$, $[CH_3CO]^+$, 8 - $[O_2]^+$.

3.1.2. *Stability of the precursor under CVD conditions*

A valuable technique for studying the stability and decomposition pathways of a precursor under CVD conditions is *in-situ* gas phase mass spectrometry. Monitoring of the precursor decomposition by-products was performed by heating the compound at 190 °C and directing its vapors to the mass spectrometer through a hot-wall quartz tube at low pressures mimicking a miniature CVD reactor setup. This setup prevents the analysis from artefacts due to the influence of sampling. The collected MS data are used to establish the composition of the gas phase as a function of equivalent process temperature in the range of 200 – 500 °C and enables to gain insight into the thermal stability and decomposition behavior of the precursor. The obtained results are displayed in Fig. 2 and are described from the lowest to the highest probed temperatures.

Increasing temperature results in a similar fragmentation behavior of all peaks in the Zr containing mass spectra. The evolution with temperature of the most intense fragment $[Zr(O^iPr)(tbaoac)_2 - CH_3]^{+\cdot}$ (fragment **1**) is shown in Fig. 2 as the representative of these peaks. Its intensity remains constant up to 260 °C before decreasing gradually until the detection limit is reached. Such similar stability upon heating indicates that all Zr containing fragments originate from the evaporation of the precursor and not from reactions in the gas phase. The upper stability temperature of 260 °C can be considered as the onset temperature of precursor thermolysis. At around 320 °C, the maximum thermolysis is achieved. No changes in the oxygen peak intensity (fragment **8**) were observed during this temperature increase indicating intramolecular decomposition of the precursor rather than a chemical reaction with oxygen showing the single source precursor properties of the compound.

Starting at around 260 °C, the increasing intensity of gaseous by-products as for instance $[O^iPr]^{+\cdot}$ (fragment **2**) indicates the cleavage of the -O^iPr group from the precursor. The intensity of the -O^iPr species reaches a maximum at approximately 310 °C and it rapidly decreases above this temperature. Fragments corresponding to hydrocarbons, e.g. $[C_2H_4]^{+\cdot}$ (fragment **5**) or $[C_3H_8]^{+\cdot}$ (fragment **6**), show a rapid increase after a latent temperature change (~330 °C) suggesting a connection to -O^iPr event at 310 °C. This correspondence reveals that the binding energy to the Zr metal center of the (tbaoac) ligand is higher compared to the -O^iPr group. This can be due to the bidentate nature and π-electron delocalized backbone of this ligand, increasing the stability of the complex. The impact of the ligand choice on physicochemical properties, such as the decomposition behavior of the heteroleptic Zr compound is thus demonstrated.

3.2. *DLI-CVD process development and thin film characterization*

ZrO_2 thin films were deposited using $[Zr(O^iPr)_2(tbaoac)_2]$ in a DLI-CVD reactor varying the deposition temperature in the

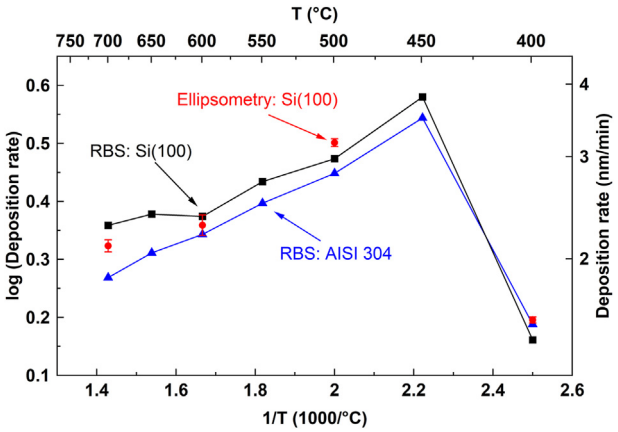

Fig. 3 – Arrhenius plot for ZrO_2 thin films deposited on Si(100) (black squares) and AISI 304 steel (blue triangles). Film thicknesses were estimated using RBS. The connection of the data points is a guidance for the eye. The red circles show the thicknesses of ZrO_2 on Si(100) estimated by ellipsometry. The error bars represent the standard deviation from the 3 × 3 measurement spot matrix.

range of 400 – 700 °C. To gain insight into the structural, compositional, and morphological features, different substrate types such as Si(100) and stainless steel AISI 304 were employed parallelly allowing a direct comparison of these characteristics, which are described as follows. For the evaluation of CPC performance, the ZrO_2 coatings on AISI 304 were selected. A representative example of the visual appearance of the ZrO_2 coatings is shown in the Supporting Information (Fig. SI 2).

3.2.1. *Deposition rates*

Fig. 3 presents the Arrhenius plot of the deposition rate of the ZrO_2 films on Si(100) and AISI 304 as a function of the inverse temperature. The film thicknesses obtained from RBS/NRA and ellipsometry (only on Si(100) substrates) used for the Arrhenius plot are listed in Table SI 2. The deposition rate values are similar on the two different types of substrates, and the deviation observed might be from the error of the thickness determination by RBS. This indicates a similar growth behavior for ZrO_2, irrespective of the selected substrate type. At the deposition temperature (T_{dep}) of 400 °C, the lowest deposition rate was around 1.5 nm/min, which rapidly increases to approximately 3.8 nm/min at 450 °C for films on both substrates. This indicates a kinetically controlled regime, which is in accordance with findings from previously reports [39,47,48].

No distinct diffusion-controlled regime is observed above 450 °C but rather a constant decrease of the deposition rates up to 700 °C. This behavior may be due to the participation of thermodynamically controlled ongoing surface reactions, which predominate over competing diffusion events. Taylor et al. [41] who used a structurally similar Zr precursor in a DLI-CVD process stated that precursor depletion on reactor walls and in the gas phase cause the decrease in the deposition rate.

3.3. *Structural analysis*

3.3.1. *Grazing-incidence XRD*

GIXRD analysis was performed for films deposited on both substrates at 400, 500, 600 and 700 °C, allowing a direct comparison of the structural features of the films, as depicted in the two diagrams of Fig. 4.

For the thin film grown at 400 °C on Si(100), only an extremely broad reflection is observed ranging from approximately $2\theta = 28.7° - 32.4°$, which could be assigned to the (111) reflection of cubic ZrO_2 (JCPDS 00-003-0640). The width of this reflection could be due of extremely small, spatially randomly distributed crystallites or an effect of the measurement setup due to the detection of the underlying substrate rather than the film itself, wherefore a clear XRD crystallinity cannot be postulated unambiguously. To give a more precise statement about the structural situation, the XRD amorphous thin film deposited at 400 C temperature was investigated using TEM, which is described later.

Between 400 and 500 °C, the films deposited on Si(100) undergo a structural change from XRD amorphous to polycrystalline, exhibiting reflections unambiguously assignable to the monoclinic (JCPDS 00-024-1165) and cubic ZrO_2 phases. This is in accordance with findings from Gould et al. [47] who investigated the structural change of ZrO_2 MOCVD growth between 400 and 500 °C. A clear distinction for the cubic reflections at 35.02°, 50.38° or 62.73° referring to the (200), (220) and (222) planes are not possible due to the overlap of the monoclinic pattern. However, the (111) and (311) reflections at 30.17° and 60.03° can be clearly assigned to the cubic ZrO_2 phase. The monoclinic phase seems to be predominant as observed from the overall higher diffraction intensity compared to the cubic crystal reflections. Interestingly, the tetragonal phase was not detected in the thin films. The rather unexpected presence of the cubic phase even at low deposition temperatures such as 500 °C is in accordance with findings of Ray et al. [49] who showed the formation of nanocrystalline cubic domains in powders. Counterintuitively, the degree of crystallinity found in the GIXRD does not increase gradually at elevated temperatures, which can be partly explained with the competing growth behavior of the two different polymorphs most likely influencing each other. Moreover, the fixed positioning of the sample relative to the X-ray beam can cause a change in the detected intensity of the crystalline domains hampering a quantitative statement on the degree of crystallinity. Notably, the higher signal-to-noise ratio at ~20° – 25° in the 500 °C processed film on Si(100) occurred due to a partial reflection of the substrate holder.

The depositions carried out on AISI 304 show a similar pattern, featuring an onset of crystallization at 500 °C with the same crystalline phases, namely monoclinic and cubic. Noteworthy, aside the extremely broad reflection at ~30.1°, only the austenite reflections were detected for the 400 °C film, originating from the stainless steel substrate. Between 500 and 700 °C, at 28.20° the (−111) reflection corresponding to the

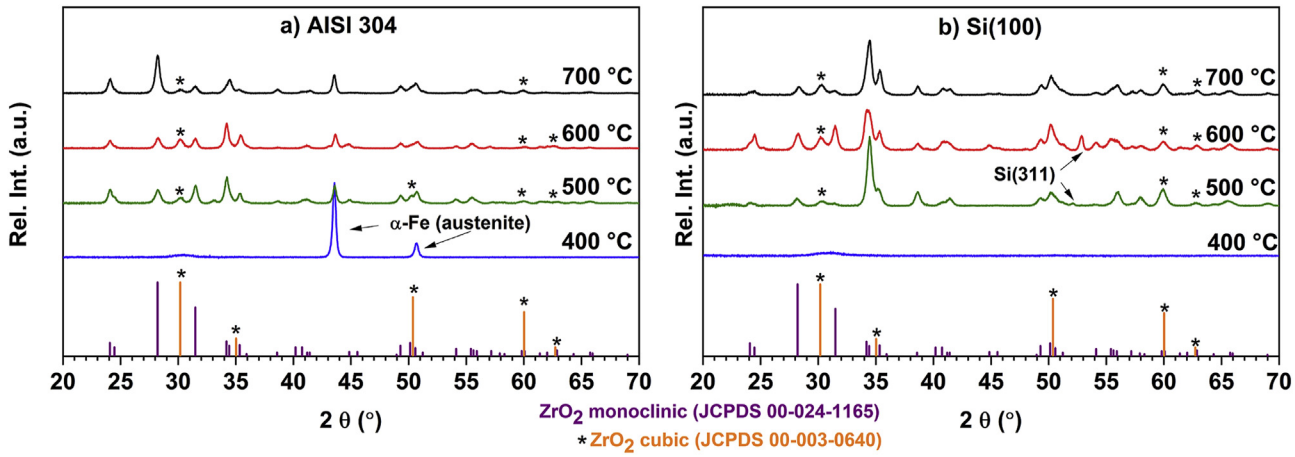

Fig. 4 – GIXRD patterns of ZrO_2 thin films on a) AISI 304 and b) Si(100) substrates. The reference powder pattern of monoclinic (JCPDS 00-024-1165) and cubic (JCPDS 00-003-0640) ZrO_2 are depicted in purple and orange color, respectively. The asterisk is to guide the eye (cubic phase).

monoclinic phase becomes more pronounced whereas an opposite trend is observed for the (002) reflection at 34.13°. The cubic phase was not found to be as pronounced as the monoclinic, but the diffractions obtained from the (111), (220) and (311) planes can be clearly assigned to this ZrO_2 phase.

3.3.2. *FT-IR ATR*

FT-IR ATR spectroscopy is a powerful tool for qualitative analysis of thin films due to the high sensitivity towards vibrations in both crystalline and amorphous material. Moreover, the detection of organic species can hint to potential residuals and impurities possibly present in the film. Consequently, FT-IR measurements for zirconia thin films on AISI 304 in the temperature range of 400 – 700 °C were carried out as depicted in Fig. 5.

The spectra exhibit characteristic vibrations in the far-IR regime (<800 cm^{-1}) originating from zirconia vibrations.

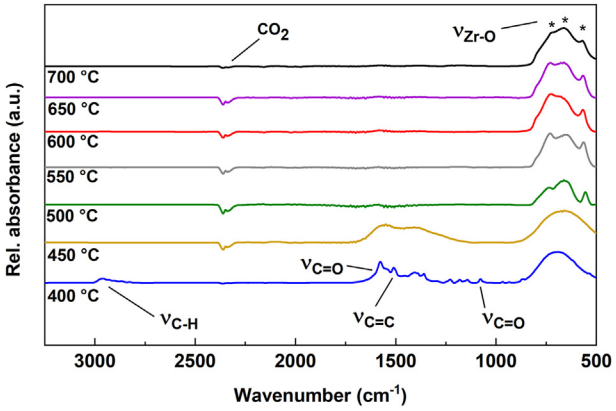

Fig. 5 – FT-IR ATR spectra of ZrO_2 thin films deposited on AISI 304 as a function of deposition temperature. The vibration at 2347 cm^{-1} recorded in each spectrum can be assigned to the characteristic CO_2 stretching vibration due to operation at ambient conditions.

Within this area, the bands located at 730, 650, and 560 cm^{-1} can be attributed to the monoclinic phase of zirconia [50].

The spectra of the 400 °C (blue graph) deposited thin films solely show a broad vibration band, which can be attributed to Zr–O, however, not allowing a clear assignment of the phase. It is reported in literature that the other two ZrO_2 polymorphs (tetragonal, cubic) are more difficult to detect, based on their higher symmetry causing fewer characteristic vibrations partly overlapping with the monoclinic ones [51].

The 400 °C film exhibits C–H stretching vibrations detected at around 2960 cm^{-1}. In both the 400 and 450 °C spectra, the pronounced yet broad vibrational bands at ~1590 cm^{-1} can be assigned to the C=O stretching mode. For the 400 °C film multiple weak vibrations occur at lower wavenumbers whereas the 450 °C film shows a broad tailing of the bands without the resolution of distinct modes. Most likely this originates from the detection of C=C and C–O vibrations as well as bending of C–H functions. These vibrations suit findings from Fleeting et al. [52] who reported IR of structurally related Zr compounds thus indicating the presence of precursor fragments or solvent residuals in the films. However, for the films deposited at 500 °C or higher temperatures, these C–H and C–C and C–O vibrational modes were not detected, indicating the absence of such ligand species, possibly reasoned by a faster desorption of these by-products or a more complete combustion reaction with O_2.

3.4. *Film composition*

3.4.1. *RBS/NRA analysis*

As discussed before in section 3.2.1., the variation of deposition temperature impacts the growth behavior of the thin film deposition. Therefore, it is likely that the composition is differing, too, as already indicated by the IR-measurements, showing carbon species incorporated in films deposited at lower temperatures. Impurity incorporation into the thin film can influence the CPC properties. Hence, the elemental composition was determined by RBS/NRA on both substrate

types and the results are summarized in Table SI 1 of the Supporting Information (SI).

Two trends can be derived from the data. First, the zirconium and oxygen (Zr/O) ratio in the films deposited at $T_{dep} \geq 500$ °C on AISI 304 is slightly increased (Zr/O = 0.6) compared to the ratio on Si(100) substrates, which is close to the ideal value of Zr/O = 0.5 indicating the stoichiometric the formation of ZrO_2 films. Second, the carbon content in the films was found to decrease drastically from 16.6 to 4.1 at.% with increasing temperature from 400 to 700 °C for depositions on Si. A similar trend is observed for the films deposited on stainless steel supporting the assumption of similar surface reactions and transport phenomena taking place during the growth on both surfaces. The higher carbon content of the depositions in the lower temperature regime could be attributed to an incomplete precursor reaction and decomposition followed by a slow desorption from the surface consequently resulting in the incorporation of ligand fragments, which were identified by means of FT-IR. Generally, the presence of the solvent (n-heptane) must be considered since it is known to be a source of carbon incorporation as well. Interestingly, in all coatings, small traces (<0.4 at.%) of Hf was detected, most likely originating from Hf metal contaminations in the $[Zr(O^iPr)_4 \cdot (HO^iPr)]$ reagent used for the synthesis of the Zr precursor.

3.4.2. *XPS analysis*

The information about the chemical species in the thin films was acquired by X-ray photoelectron spectroscopy (XPS) for films deposited on Si(100) at 400, 500 and 700 °C, respectively. Due to the surface sensitivity and low penetration depth of this measurement technique, survey, and core level spectra (Zr3d, O1s, C1s) were collected from the films as introduced and after 30 and 430 s Ar^+ sputtering. Exemplarily, the survey and 30 and 430 s sputtered ZrO_2 film deposited at 500 °C and Zr3d core level spectra of the 30 s sputtered ZrO_2 thin films grown at selected temperatures are shown in Fig. 6 and Fig. 7, respectively. The detailed XPS data is provided in the SI in Fig. SI 4 - Fig. SI 7, and Table SI 3.

In the survey spectra signals related to presence of elements namely Zr, O and C were observed in the expected regions. The absence of Si 2s (151 eV) and Si 2p (99 eV) photoelectron lines proves that during the 430 s sputter time the films were not penetrate entirely therefore providing insights about the chemical situation of the thin film bulk material.

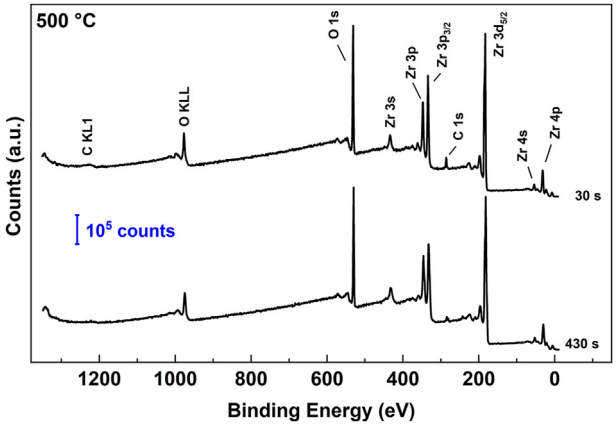

Fig. 6 – XPS survey spectra of ZrO_2 on Si(100) deposited at 500 °C after 30 s (top) and 430 s (bottom) of sputtering.

The Zr3d core level spectra depicted in Fig. 7 exhibit four distinct species for the measured temperature. Firstly, the asymmetric $Zr3d_{3/2}$ and $Zr3d_{5/2}$ peaks at 184.5 and 182.2 eV feature the typical spin–orbit doublets with Δ = ~2.4 eV separation indicating the formation of Zr^{4+} oxide (ZrO_2) material [2,53,54]. Compared to literature reports, the binding energies were found to be slightly shifted to higher energies. This can be best explained by the formation of oxygen deficient states in the material, due to preferential oxygen sputtering causing a more ionic nature of the Zr–O bonds [55]. Moreover, the sputtering causes the formation of suboxides due to an reduction of Zr^{4+} species resulting in the detection of $Zr3d_{3/2}$ and $Zr3d_{5/2}$ suboxides (green colored peaks) especially at longer sputter times (see Fig. SI 5) [56]. Interestingly, the other two species, $Zr3d_{3/2}$ $Zr3d_{5/2}$ carbides and oxycarbides, were detected in thin films normally only accessible using high temperature CVD or plasma CVD processes [57].

The C1s core level spectra (Fig. SI 6) reveal the presence of aliphatic C, C–O and O=C–O species at 284.4, 286.2 and 288.7 eV for all deposition temperatures. Due to a strong reduction of the carbon content from the as introduced to the 430 s sputtered films, these species can be partly attributed to adventitious carbon at the surface. However, especially for lower deposition temperatures, there is a strong indication of incorporation of decomposed ligand or solvent fragments, which is evidenced from the higher carbon content. Furthermore, these findings are in line with the data obtained from the O1s core level spectra (Fig. SI 7). Apart from the oxide peak at 530.4 eV being the most pronounced, the contributions from organic C=O (532.2 eV) and C–O (533.2 eV) species were found to gradually decrease at higher temperatures and longer sputter times. This trend agrees with the findings from RBS/NRA. Interestingly, the peaks at the low-energy side around 282.2 eV are assignable to carbide species, thus supporting the findings from the Zr core levels.

3.5. *Surface and interface characterization*

3.5.1. *SEM and AFM analysis*

The appropriate protection performance of a metal part against corrosion depends among others on the morphology of the coating since the latter is directly exposed to the corrosive environment. Logically, the corrosion resistant film should cover the entire surface without gaps and ideally should not feature grain boundaries. Grain boundaries is a potential weak spot since the corrosive medium may diffuse and corrode the material. Furthermore, the surface of the AISI 304 can be oxidized upon thermal treatment in oxidizing atmosphere, which has been shown to modify the substrate surface and could impact the CPC behavior [58,59]. In this context, SEM and AFM measurements were performed on specific ZrO_2 films on AISI 304, and the data are depicted in Fig. 8.

Both techniques show a closed film covering the observed areas. At a first glance, the 400 °C grown ZrO_2 surface exhibits a different morphology compared to those of films deposited

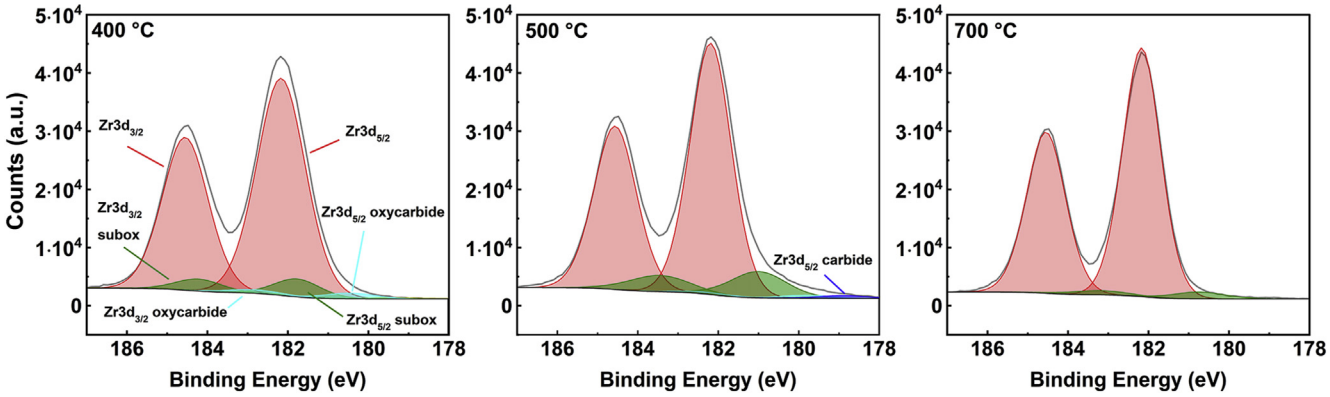

Fig. 7 – XPS Zr3d core-level spectra of ZrO_2 thin films deposited on Si(100) at 400 °C, 500 °C and 700 °C after 30 s of Ar^+ (500 eV) sputtering.

at higher temperatures. It features round shaped agglomerates suggesting an isotropic growth of ZrO_2 film. Although a direct comparison between the SEM and GIXRD is not straightforward, the amorphous rather than polycrystalline nature of the 400 °C film can be assumed. Notably, on top of those agglomerates, other features exhibiting a different morphological appearance were detected. Due to the randomly, branched distribution on the top of the surface it can be most likely attributed to precursor residuals and unreacted precursor species than ZrO_2 material. This is supported by the findings from IR and XPS, which show an increased level of C content at the top of the films. At 500 and 600 °C, the ZrO_2 morphology changes significantly and the typical arrowhead-like shaped crystallites [47] are formed during the deposition, which transform to more needle-like at 700 °C. The observed surface morphologies reveal that the density of grain boundaries within the film increases upon increasing the deposition temperature.

For the scanned [(5 μm)^2] areas, the RMS for the 400 °C deposited films was calculated to be considerably lower than the films deposited at higher temperatures with RMS values of 13.2 nm (140 nm thickness, 400 °C), 24.9 nm (250 nm thickness, 500 °C), 35.5 nm (200 nm thickness, 600 °C) and 29.9 nm (170 nm thickness, 700 °C), respectively, supporting the observations from SEM. Notably, the 400 °C RMS value is close to the value of the bare AISI 304 substrate (9.81 nm, Fig. SI 8) demonstrating that the film morphology follows the topography of the uncoated whereas at $T_{dep} \geq 500$ °C the mode of the crystalline growth already takes over the topography of the surface.

3.5.2. *Transmission electron microscopy*

The interface and structure of the ZrO_2 layers on AISI 304 were investigated by cross-sectional bright field (BF) TEM, high-resolution TEM (HRTEM) and selective area electron diffraction (SAED). As representative examples, data gathered from thin films deposited at 400 and 500 °C are displayed in Fig. 9.

The 400 °C deposited ZrO_2 film features a dense and structureless material at a first sight. However, dark spots interspersed in the region near the interface indicate the formation of nanocrystallites smaller than 10 nm. Consequently, SAED of this region was carried out, revealing a halo-like diffraction pattern resulting from randomly oriented crystallites. A closer analysis shows distinct diffraction spots along the circles

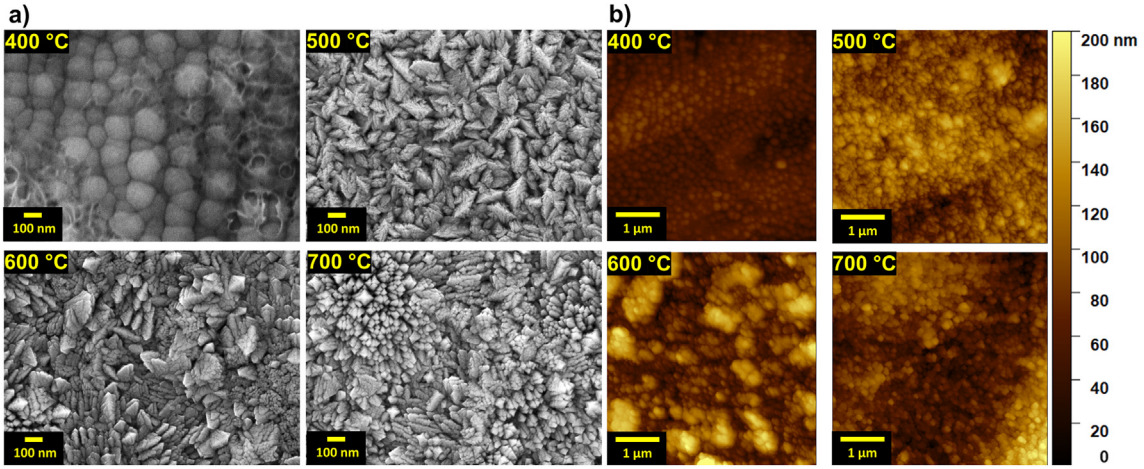

Fig. 8 – a) SEM images (left) and b) AFM micrographs (right) of ZrO_2 thin films deposited on AISI 304 at selected temperatures.

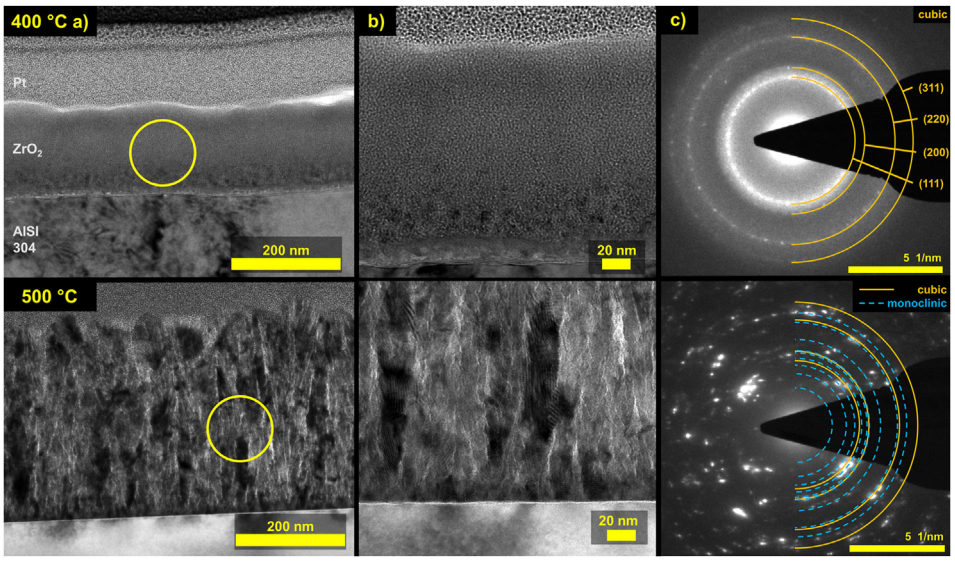

Fig. 9 – a) BF-TEM, b) HR-TEM and c) SAED of 400 °C (top) and 500 °C (bottom) deposited ZrO_2 on AISI 304. The yellow rings in a) display the areas for the respective SAED measurements shown in c). The colored half circles in the SAED 400 °C image display the pattern of cubic phase of ZrO_2, the dashed blue and solid orange lines represent the cubic and monoclinic phase, respectively. For the sake of clarity, only reflexes with rel. intensity >12% are depicted for the monoclinic phase.

correlating to the cubic phase of ZrO_2. Therefore, it can be deduced that although the layer is mainly amorphous in nature, a small degree of polycrystallinity of cubic phase is present. This observation is most likely attributable to the effect of critically small grain sizes causing a change in the nucleation behavior to the cubic phase [60]. Furthermore, from the HR TEM it is visible that these cubic ZrO_2 domains start to appear after the growth of the first 20 nm of film, indicating a different initial growth behavior of the ZrO_2 on the AISI 304 substrate at 400 °C. Notably, the crystallites were detected approximately within the first 40 nm of the ZrO_2 material, which could be attributed to annealing effects during the process.

The 500 °C ZrO_2 film, on the contrary, clearly shows a structure along the depth profile being best described as branched columnar. The SAED pattern shows clusters of diffraction spots rather than well-defined spots occurring probably due to a mosaic arrangement of the crystallites [61]. Although a certain degree of polycrystallinity in form of ring formation is visible, the crystallites of the observed area are assignable to the monoclinic phase and are of relatively high order, which supports the findings from GIXRD measurements (section 3.3.1.).

3.6. *Electrochemical measurements*

Electrochemical impedance spectroscopy (EIS) is a valuable tool to evaluate the performance of corrosion protective coatings [62–64]. In the framework of this study, EIS was employed to characterize the ZrO_2 coatings deposited onto AISI 304 at different temperatures (400 – 700 °C) in NaCl solution. To confirm the stability of the system, the open circuit potential (OCP) was recorded before starting the EIS experiments. As depicted in Fig. SI 9, the OCP is stable within 120 s for all coatings, indicating that a steady state is reached within the measurement time.

Among the tested coatings, the noblest OCP was observed for the coating deposited at 400 °C and the respective OCP stabilized much faster. For the coatings deposited at higher temperature (500 – 700 °C), small potential oscillations were detected. Cabrini et al. [65] found that such oscillations are probably due to the existence of a diffusion path inside the porous coating. These findings are in accordance with the above-mentioned AFM roughness and TEM investigations (section 3.5.2.), which showed that the microstructure of the amorphous coating (400 °C) is significantly denser and more homogeneous than the microstructure of the crystalline ones.

Fig. 10 (a, b, c) presents the Nyquist and Bode plots of the zirconia coatings deposited at different temperatures (400 – 700 °C). Apparently, the impedance spectra of all coatings have similar tendency except that deposited at 400 °C, indicating a different electrochemical behavior for amorphous (400 °C) and crystalline (500, 600, 700 °C) coatings. For the amorphous coating, the presence of two semicircles in the Nyquist plot (Fig. 10 a) and double peaks in the corresponding Bode phase plot (Fig. 10 c) suggests two time constants associated to the electrochemical process at the electrolyte/coating/substrate interface: A depressed semicircle at higher frequencies and a straight line at intermediate and low frequencies.

In contrast, all crystalline coatings show a single time constant with a single semicircle in the Nyquist plot. In the EIS measurements, the curves in the Nyquist plot (Fig. 10 a) tend to display a shape of distorted semicircle or a straight line, whose slope is not equal to one. Zhao et al. [66] attributed that to intrinsic or electrochemical properties of electrodes, electrolytes, and the conditions of the experiments. Since the diameter of the semicircle in the Nyquist plot partly implies the corrosive resistance, the larger semicircle diameter of the coating deposited at 500 °C indicates a higher corrosion

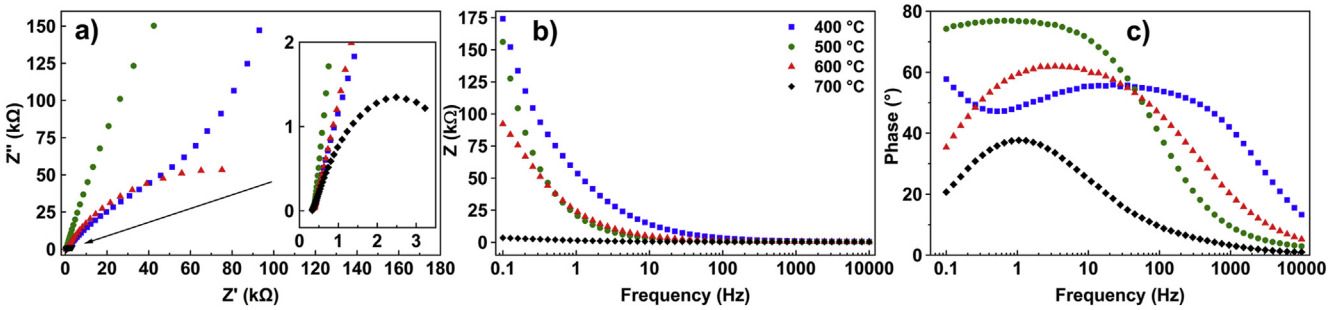

Fig. 10 – Nyquist diagrams a), Bode plot b) and Bode phase plot c) for ZrO_2 coatings onto AISI 304 deposited at 400 C–700 °C.

resistance [30]. In the same sequence, the smallest diameter of the semicircle was obtained for the coating deposited at 700 °C confirming its weakest corrosion properties.

The impedance modulus |Z|, which serves as a figure of merit for the performance of anticorrosion films [67] was found to be higher for the amorphous film (400 °C) over the whole frequency range, suggesting the best barrier properties of this film (Fig. 10 b). Notably, this could be partly influenced by the elevated carbon content, which hampers the crystalline growth of material, thus leading to more dense films.

In the phase angle plot (Fig. 10c), the two time constants can be ascribed to a bi-layer configuration of the coating: An outer porous layer with broad time constant in the range of $1 - 10^4$ Hz, and denser inner oxide layer in the range of 1 – 0.1 Hz. The obtained results are in a good agreement with the findings of Yao et al. [68] who established that the ceramic ZrO_2 coatings present

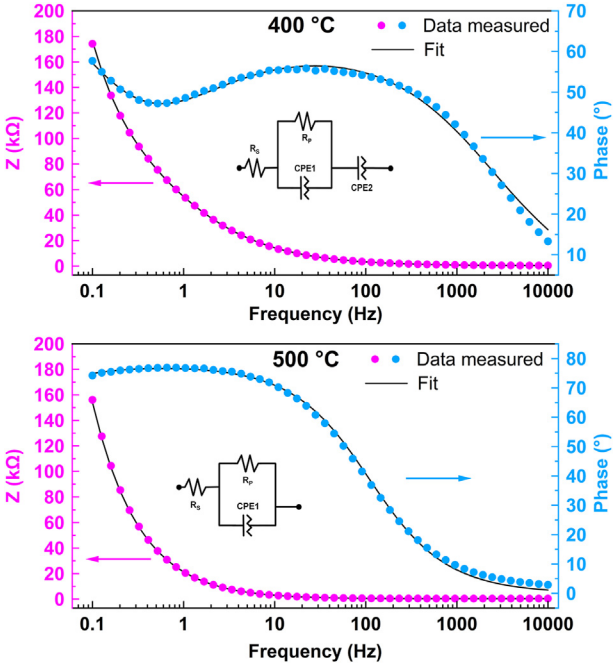

Fig. 11 – Fitted Bode plots of ZrO_2 films deposited at 400 °C (amorphous) and 500 °C (crystalline) in NaCl solution at 40 °C. The corresponding equivalent circuits are displayed as insets.

a double-layer structure with the loose and porous outer layer and the compact inner layer.

The EIS data was simulated and the fitted equivalent circuits for the amorphous (400 °C) and crystalline (500 °C) thin films are presented in Fig. 11 and Fig. SI 9. A close agreement of the proposed models and the experimental results is observed. This, and the low χ^2 values corroborate the accuracy of the proposed models. In Table 1, the fit values for the elemental parameters in various equivalent circuits describing the electrical properties of the varying electrode/electrolyte interface are presented.

For the amorphous coating (400 °C), the electrical circuit is composed of two resistors and two capacitive elements. R_s can be assigned to a system resistance that includes the electrolyte resistance as well as other instrument factors, contributing especially at high frequencies [69]. Due to roughness and inhomogeneities such as composition or structure changes, ideal capacitors fail for the modulation. Hence, non-ideal capacitors, so called constant phase elements (CPEs) were applied. The mathematical expression for impedance of a CPE is given by the following Equation (2) [70]:

$$Z_{CPE} = \frac{1}{Q \cdot (j\omega)^N} \quad (2)$$

where Z_{CPE} (Ω) is the impedance of the CPE, Q is the admittance of CPE ($S \cdot s^N$) and accounts for conduction paths for water uptake, ionic migration, and salt intrusion within the coatings. The value of N for CPE is 0–1: CPE operates as pure resistor and as a pure capacitor for N values equal to 0 and 1, respectively.

R_p represents the pore resistance and CPE1 stands for the coating capacitance. As mentioned by Zhang et al. [71], the parameters R_p and CPE1 (Fig. 11) are related to the outer layer, which corresponds to the upper layer of the ZrO_2 coating. We attribute the existence of CPE2 to inhomogeneities in the coating with electrolyte uptake, which is in line with proposed physical models of substrate/coating/electrolyte systems [72,73]. The obtained finding is in good agreement with the assumption of Amand et al. [74], in which the coating uptakes electrolyte to an extent that progressively decreases from the coating/electrolyte interface to the substrate/coating interface, where it becomes negligible.

It is well known that the CPE can be used to account for the roughness of the solid electrode, whereby the lower the value of the exponent (N), the rougher the electrode surface [75]. In

Table 1 – EIS fitting parameters for equivalent circuits of ZrO_2 coatings deposited at 400–700 °C onto AISI 304.

T_{dep} (°C)	Film Thickness (nm)	R_s (Ω)	R_P (kΩ)	CPE1		CPE2	
				Q ($\mu S \cdot s^N$)	N	Q ($\mu S \cdot s^N$)	N
400	168	358	88	5.0	0.66	11.6	0.91
500	304	363	1710	10.2	0.86	–	–
600	247	378	160	10.8	0.73	–	–
700	234	304	5	247	0.66	–	–

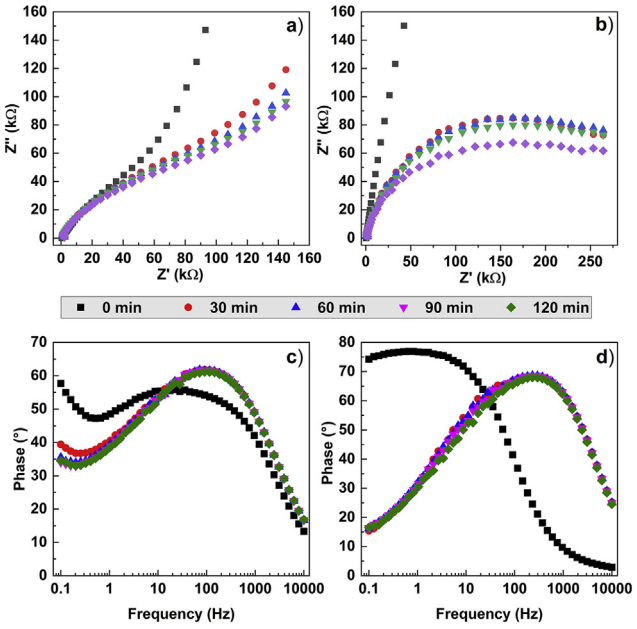

Fig. 12 – Nyquist (top, a, b) and Bode plots (bottom, b, c) with different immersion time (0 min–120 min) for ZrO_2 on AISI 304 at 400 °C (a, c) and 500 °C (b, d).

the present measurements, the higher N value of CPE2 (N = 0.91) compared to that of CPE1 (N = 0.66), indicates less defects/pinholes and higher compactness of the inner layer of the amorphous film. That is to say, the inner film/stainless steel interface operates approximately as an ideal capacitor, which suggests better corrosion barrier. The characteristics of CPE2 are distinctly closer to a pure capacitor.

The EIS measurements of the crystalline coatings (500, 600 and 700 °C) are fitted to the equivalent circuit of system resistance (R_s) connected with one-time constants in parallel arrangement of R_p and a capacitive part of the coating CPE1 (Fig. 11). Obviously, CPE2 does not exist for the crystalline coatings, suggesting the formation of a single, porous ZrO_2 layer. Drawing a direct interconnection between pore resistance and corrosion performance may be complicated. However, Zhang et al. [71] reported that R_p values can be used to express the integrity of coating such as adherence, pore and crack existence or stability. For the crystalline coatings, the highest R_p value was determined for the coating deposited at 500 °C, where lower porosity can be expected. The lowest R_p was related to the coating deposited at 700 °C, which is probably due to many defects and/or pinholes developed at higher deposition temperature.

To further compare the stability of amorphous and crystalline coatings, EIS immersion tests of two selected coatings deposited at 400 and 500 °C was performed. Fig. 12 shows the evolution of the Nyquist plots for both coatings during immersion tests in 0.1 wt.% NaCl aqueous solution (from 30 to 120 min). A fast drop of impedance is marked after the first 30 min for both coatings (Fig. 12 a, b) and a depressed form of impedance Nyquist diagrams is observed due to the initial electrolyte uptake by the coating and the diffusion of electrolyte inside into coating layer. However, with longer than 30 min immersion times, only small changes in the Nyquist plot are noticed, indicating that the electrolyte uptake reaches a stationary state. It is worth noting that no evidence of coating damage was detected, as there are no additional loops in the impedance diagrams during the whole immersion period. This is also a strong indication that the electrolyte does not permeate to the base substrate.

In the Bode diagram (Fig. 12 c), the maximum phase angle of the amorphous coating increases after immersion of 30 min and remains nearly constant for longer immersion times, namely 60 – 120 min. However, the phase angle decreases at lower frequencies, indicating to the diffusion of electrolyte through the outer coating layer. The situation is opposite for the crystalline coating, where the maximum phase angle is found to be lower for coatings at all immersion times, indicating a poor barrier performance (Fig. 12 d). At low frequency (0.1 Hz), the phase angle reaches a value lower than 20°, indicating that the coating has been completely permeated by electrolyte [76].

The EIS measurements indicate better corrosion protection for ZrO_2 coatings deposited at 400 °C compared to those deposited at and above 500 °C. Combined with the XRD results (Section 3.3.1) and TEM investigations (Section 3.5.2), it is assumed that the crystalline coatings contain more pores and defects due to their higher degree of crystallinity and the resulting coarse microstructure. Perhaps, a coupling of stainless-steel to the ZrO_2 could likely be present, and an in-depth study of this correlation will be of imminent interest for our future investigations.

4. Conclusion

Within the framework of this study [$Zr(OiPr)_2(tbaoac)_2$] was successfully applied as precursor for coating ZrO_2 thin films on stainless steel AISI 304 substrates to evaluate their application as corrosion protective layers. The thermal evaluation and in-situ gas phase compositional analysis revealed a high kinetic stability of the

$[Zr(O^iPr)_2(tbaoac)_2]$ precursor at temperatures up to 260 °C ensuring an intact transport of the precursor vapor to the deposition zone without prior decomposition as a consequence of thermolysis. This robust behaviour allowed developing a DLI-CVD process for the fabrication of ZrO_2 thin films on Si(100) and stainless steel AISI 304. The structural and morphological characteristics of these films were systematically investigated by varying the deposition temperature in the range of 400 – 700 °C. The deposition rate, composition and structure of the films are comparable on both types of substrates featuring the highest deposition rates at 450 °C (~3.8 nm/min) and the presence of two ZrO_2 phases, namely monoclinic and cubic. An increase in the RMS roughness from 400 °C to higher deposition temperatures was observed, explainable with the change of the structural growth of ZrO_2. These findings were supported by GIXRD showing a change in the growth of polycrystalline ZrO_2. At 400 °C, approximately 17 at.% carbon was detected in RBS/NRA most probably occurring due to incomplete precursor reaction and residuals at the surface as elucidated via IR. SAED and TEM of the 400 °C film highlighted the existence of fine crystallites of polycrystalline cubic ZrO_2. From SEM and GIXRD this feature was not observed showing an amorphous nature of the film at such low temperatures.

EIS measurements reveal better corrosion protection performance of the coating deposited at 400 °C in comparison with the films deposited at higher temperature (500 – 700 °C). For longer immersion times (30 – 120 min), the corrosion protection of the amorphous coating (400 °C) remains intact, while the crystalline thin film (500 °C) shows poor protecting behavior with the electrolyte diffusing towards the substrate. Thus, we could demonstrate a potential process design for a thin, dense, and efficient corrosion protection coating deposited at low temperatures, which could be of interest for the application on steel tools used in the injection molding of plastic parts.

Our study highlights the importance of the thoughtful correlation between all the vital steps for the successful fabrication of ZrO_2 thin films with improved corrosion protection performance using CVD: Starting from the rational choice of the precursor to the careful process development and thorough analysis, which ultimately results in formation of the ZrO_2 material with tailored surface and compositional characteristics. This target-oriented approach outplays the "trial-and-error" method for the CVD of CPCs and furthermore gives highly relevant insights into the growth characteristics and thin film properties motivating us to adapt this approach to other corrosion protection materials such as YSZ or Al_2O_3, which we intend to explore in the near future.

Declaration of Competing Interest

The authors declare that they have no known competing financial interests or personal relationships that could have appeared to influence the work reported in this paper.

Acknowledgements

The authors from Ruhr University Bochum (RUB) and Fachhochschule Dortmund thank the Federal Ministry of Education and Research Germany (BMBF, Project 03INT505AB CAP-CPC) for funding the work. The authors from CIRIMAT (CNRS) thank Bpifrance for funding the work through the project 0099186 of the Fonds unique interministeriel (FUI) 25th call. MS study of the precursor was supported by CNRS and RFBR through grants PRC 1986/2018 and 18-53-15005, which is acknowledged. We are indebted to Xiao Wang for AFM measurements, which were carried out at the Center for interface dominated materials (ZGH, RUB).

Appendix A. Supplementary data

Supplementary data to this article can be found online at https://doi.org/10.1016/j.jmrt.2021.05.068.

REFERENCES

[1] Panda D, Tseng T-Y. Growth, dielectric properties, and memory device applications of ZrO_2 thin films. Thin Solid Films 2013;531:1–20. https://doi.org/10.1016/j.tsf.2013.01.004.
[2] Son B-G, Je SY, Kim HJ, Lee C-K, Lee C-K, Hwang AY, et al. High-performance In-Zn-O thin-film transistors with a soluble processed ZrO_2 gate insulator. Phys Status Solidi RRL 2013;7(7):485–8. https://doi.org/10.1002/pssr.201307128.
[3] Shin WJ, Huang W-H, Tao M. Low-cost spray-deposited ZrO_2 for antireflection in Si solar cells. Mater Chem Phys 2019;230:37–43. https://doi.org/10.1016/j.matchemphys.2019.03.063.
[4] Kim M, DiMaggio C, Salley SO, Simon Ng KY. A new generation of zirconia supported metal oxide catalysts for converting low grade renewable feedstocks to biodiesel. Bioresour Technol 2012;118:37–42. https://doi.org/10.1016/j.biortech.2012.04.035.
[5] Noichi H, Uddin A, Sasaoka E. Steam reforming of naphthalene as model biomass tar over iron–aluminum and iron–zirconium oxide catalyst catalysts. Fuel Process Technol 2010;91(11):1609–16. https://doi.org/10.1016/j.fuproc.2010.06.009.
[6] Tsampas MN, Sapountzi FM, Vernoux P. Applications of yttria stabilized zirconia (YSZ) in catalysis. Catal Sci Technol 2015;5(11):4884–900. https://doi.org/10.1039/C5CY00739A.
[7] Spirig JV, Ramamoorthy R, Akbar SA, Routbort JL, Singh D, Dutta PK. High temperature zirconia oxygen sensor with sealed metal/metal oxide internal reference. Sens Actuators, B 2007;124(1):192–201. https://doi.org/10.1016/j.snb.2006.12.022.
[8] Garcia JV, Goto T. Thermal barrier coatings produced by chemical vapor deposition. Sci Technol Adv Mater 2003;4(4):397–402. https://doi.org/10.1016/S1468-6996(03)00048-2.
[9] Fu Y, Shao C, Cai C, Wang Y, Zhou Y, Zhou G. Temperature induced structure degradation of yttria-stabilized zirconia thermal barrier coatings. Surf Coating Technol 2018;351:21–8. https://doi.org/10.1016/j.surfcoat.2018.07.057.
[10] Deng Z-Y, Ferreira JM, Tanaka Y, Isoda Y. Microstructure and thermal conductivity of porous ZrO_2 ceramics. Acta Mater

2007;55(11):3663–9. https://doi.org/10.1016/j.actamat.2007.02.014.
[11] Liu Q, Huang S, He A. Composite ceramics thermal barrier coatings of yttria stabilized zirconia for aero-engines. J Mater Sci Technol 2019;35(12):2814–23. https://doi.org/10.1016/j.jmst.2019.08.003.
[12] Thurn G, Scheider GA, Bahr H-A, Aldinger F. Toughness anisotropy and damage behavior of plasma sprayed ZrO_2 thermal barrier coatings. Surf Coating Technol 2000;123:147–58. https://doi.org/10.1016/S0257-8972(99)00528-9.
[13] Ishak M, editor. Joining technologies. Rijeka: InTech; 2016.
[14] Atik M, 'Kha CR, Lima Neto P de, Avaca LA, Aegerter MA, Zarzycki J. Protection of 316L stainless steel by zirconia sol-gel coatings in 15 % H_2SO_4 solutions. J Mater Sci Lett 1995;14:178–81. https://doi.org/10.1007/BF00318248.
[15] Atik M, Zarzycki J, R'Kha C. Protection of ferritic stainless steel against oxidation by zirconia coatings. J Mater Sci Lett 1994;13:266–9. https://doi.org/10.1007/BF00571772.
[16] Li H, Liang K, Mei L, Gu S, Wang S. Oxidation protection of mild steel by zirconia sol–gel coatings. Mater Lett 2001;51:320–4.
[17] Norouzi M, Afrasiabi Garekani A. Corrosion protection by zirconia-based thin films deposited by a sol–gel spin coating method. Ceram Int 2014;40(2):2857–61. https://doi.org/10.1016/j.ceramint.2013.10.027.
[18] Yu J, Ji G, Liu Q, Zhang J, Shi Z. Effect of sol-gel ZrO_2 films on corrosion behavior of the 304 stainless steel in coal-gases environment at high temperature. Surf Coating Technol 2017;331:21–6. https://doi.org/10.1016/j.surfcoat.2017.10.037.
[19] Stambolova I, Dimitrov O, Vassilev S, Yordanov St, Blaskov V, Boshkov N, et al. Preparation of newly developed CeO_2/ZrO_2 multilayers: effect of the treatment temperature on the structure and corrosion performance of stainless steel. J Alloys Compd 2019;806:1357–67. https://doi.org/10.1016/j.jallcom.2019.07.308.
[20] Lei Z, Zhang Q, Zhu X, Ma D, Ma F, Song Z, et al. Corrosion performance of ZrN/ZrO_2 multilayer coatings deposited on 304 stainless steel using multi-arc ion plating. Appl Surf Sci 2018;431:170–6. https://doi.org/10.1016/j.apsusc.2017.06.273.
[21] Izquierdo J, Bolat G, Cimpoesu N, Trinca LC, Mareci D, Souto RM. Electrochemical characterization of pulsed layer deposited hydroxyapatite-zirconia layers on $Ti_{21}Nb_{15}Ta_6Zr$ alloy for biomedical application. Appl Surf Sci 2016;385:368–78. https://doi.org/10.1016/j.apsusc.2016.05.130.
[22] Cubillos GI, Bethencourt M, Olaya JJ. Corrosion resistance of zirconium oxynitride coatings deposited via DC unbalanced magnetron sputtering and spray pyrolysis-nitriding. Appl Surf Sci 2015;327:288–95. https://doi.org/10.1016/j.apsusc.2014.11.168.
[23] Cheng Z, Yang J, Shao F, Zhong X, Zhao H, Zhuang Y, et al. Thermal stability of YSZ coatings deposited by plasma spray–physical vapor deposition. Coatings 2019;9(8):464. https://doi.org/10.3390/coatings9080464.
[24] Harder BJ, Zhu D, Schmitt MP, Wolfe DE. Microstructural effects and properties of non-line-of-sight coating processing via plasma spray-physical vapor deposition. J Therm Spray Technol 2017;26(6):1052–61. https://doi.org/10.1007/s11666-017-0570-5.
[25] Liu M-J, Zhang M, Zhang X-F, Li G-R, Zhang Q, Li C-X, et al. Transport and deposition behaviors of vapor coating materials in plasma spray-physical vapor deposition. Appl Surf Sci 2019;486:80–92. https://doi.org/10.1016/j.apsusc.2019.04.224.
[26] He W, Mauer G, Sohn YJ, Schwedt A, Guillon O, Vaßen R. Investigation on growth mechanisms of columnar structured YSZ coatings in Plasma Spray-Physical Vapor Deposition (PS-PVD). J Eur Ceram Soc 2019;39(10):3129–38. https://doi.org/10.1016/j.jeurceramsoc.2019.04.003.
[27] Hospach A, Mauer G, Vaßen R, Stöver D. Columnar-structured thermal barrier coatings (TBCs) by thin film low-pressure plasma spraying (LPPS-TF). J Therm Spray Technol 2011;20(1–2):116–20. https://doi.org/10.1007/s11666-010-9549-1.
[28] Panjan Drnovšek, Gselman Čekada, Bončina Merl. Influence of growth defects on the corrosion resistance of sputter-deposited TiAlN hard coatings. Coatings 2019;9(8):511. https://doi.org/10.3390/coatings9080511.
[29] Panjan P, Drnovšek A, Gselman P, Čekada M, Panjan M. Review of growth defects in thin films prepared by PVD techniques. Coatings 2020;10(5):447. https://doi.org/10.3390/coatings10050447.
[30] Abd El-Lateef HM, Khalaf MM. Corrosion resistance of ZrO_2–TiO_2 nanocomposite multilayer thin films coated on carbon steel in hydrochloric acid solution. Mater Char 2015;108:29–41. https://doi.org/10.1016/j.matchar.2015.08.010.
[31] Perdomo LF, Lima-Neto P de, Aegerter MA, Avaca LA. Sol-gel deposition of ZrO2 films in air and in oxygen-free atmospheres for chemical protection of 304 stainless steel: a comparative corrosion study. J Sol Gel Sci Technol 1999;15(1):87–91. https://doi.org/10.1023/A:1008769231899.
[32] Wang D, Bierwagen GP. Sol–gel coatings on metals for corrosion protection. Prog Org Coating 2009;64(4):327–38. https://doi.org/10.1016/j.porgcoat.2008.08.010.
[33] Carter CB, Norton MG. Ceramic materials: science and engineering. New York: Springer; 2007.
[34] Espinoza-Pérez LJ, López-Honorato E, González LA. Development of ZrO_2 and YSZ coatings deposited by PE-CVD below 800 °C for the protection of Ni alloys. Ceram Int 2020;46(10):15621–30. https://doi.org/10.1016/j.ceramint.2020.03.109.
[35] Grehk TM, Engkvist J, Bexell U, Richter JH, Karlsson PG, Sandell A. Initial stages of metal-organic chemical-vapor deposition of ZrO_2 on a FeCrAl alloy. Thin Solid Films 2008;516(6):875–9. https://doi.org/10.1016/j.tsf.2007.04.048.
[36] Bradley DC. Metal alkoxides as precursors for electronic and ceramic materials. Chem Rev 1989;89(6):1317–22. https://doi.org/10.1021/cr00096a004.
[37] Si J, Desu SB. Metal-organic chemical vapor deposition of ZrO_2 films using $Zr(thd)_4$ as precursors. J Mater Res 1994;9(7):1721–7. https://doi.org/10.1557/JMR.1994.1721.
[38] Thomas R, Milanov A, Bhakta R, Patil U, Winter M, Ehrhart P, et al. Liquid-injection MOCVD of ZrO_2 thin films using zirconium bis(diethlyamido)-bis(di-tert-butylmalonato) as a novel precursor. Chem Vap Depos 2006;12(5):295–300. https://doi.org/10.1002/cvde.200506481.
[39] Patil U, Thomas R, Milanov A, Bhakta R, Ehrhart P, Waser R, et al. MOCVD of ZrO_2 and HfO_2 thin films from modified monomeric precursors. Chem Vap Depos 2006;12(2–3):172–80. https://doi.org/10.1002/cvde.200506394.
[40] Williams PA, Roberts JL, Jones AC, Chalker PR, Tobin NL, Bickley JF, et al. Novel mononuclear alkoxide precursors for the MOCVD of ZrO_2 and HfO_2 thin films. Chem Vap Depos 2002;8(4):163–70. https://doi.org/10.1002/1521-3862(20020704)8:4<163:aid-cvde163>3.0.co;2-v.
[41] Taylor S, Williams PA, Robert JL, Jones AC, Chalker PR. HfO_2 and ZrO_2 alternative gate dielectrics for silicon devices by liquid injection chemical vapour deposition. Electron Lett 2002;38(21):1285. https://doi.org/10.1049/el:20020801.
[42] Patil U, Winter M, Becker H-W, Devi A. Synthesis and structure of mixed isopropoxide–β-ketoester and β-ketoamide zirconium complexes: potential precursors for

MOCVD of ZrO_2. J Mater Chem 2003;13(9):2177–84. https://doi.org/10.1039/B304419J.
[43] Kunte GV, Shivashankar SA, Umarji AM. Thermogravimetric evaluation of the suitability of precursors for MOCVD. Meas Sci Technol 2008;19(2):25704. https://doi.org/10.1088/0957-0233/19/2/025704.
[44] Mayer M. SIMNRA user's guide: report IIP 9/113. Germany: Garching; 1997.
[45] Tokutaka H, Ishihara N, Nishimori K, Kishida S, Isomoto K. Background removal in X-ray photoelectron spectroscopy. Surf Interface Anal 1992;18(10):697–704. https://doi.org/10.1002/sia.740181002.
[46] Price DM. Vapor pressure determination by thermogravimetry. Thermochim Acta 2001;367–368:253–62. https://doi.org/10.1016/S0040-6031(00)00676-6.
[47] Gould BJ, Povey IM, Pemble ME, Flavell WR. Chemical vapour deposition of ZrO_2 thin films monitored by IR spectroscopy. J Mater Chem 1994;4(12):1815. https://doi.org/10.1039/JM9940401815.
[48] Morstein M, Pozsgai I, Spencer ND. Composition and microstructure of zirconia films obtained by MOCVD with a new, liquid, mixed acetylacetonato-alcoholato precursor. Chem Vap Depos 1999;5(4):151–8. https://doi.org/10.1002/(SICI)1521-3862(199908)5:4<151:aid-cvde151>3.0.co;2-9.
[49] Ray JC, Pati RK, Pramanik P. Chemical synthesis and structural characterization of nanocrystalline powders of pure zirconia and yttria stabilized zirconia (YSZ). J Eur Ceram Soc 2000;20(9):1289–95. https://doi.org/10.1016/S0955-2219(99)00293-9.
[50] Fernández López E, Sánchez Escribano V, Panizza M, Carnasciali MM, Busca G. Vibrational and electronic spectroscopic properties of zirconia powders. J Mater Chem 2001;11(7):1891–7. https://doi.org/10.1039/b100909p.
[51] Phillippi CM, Mazdiyasni KS. Infrared and Raman spectra of zirconia polymorphs. J Am Ceram Soc 1971;54:254–8. https://doi.org/10.1111/j.1151-2916.1971.tb12283.x.
[52] Fleeting KA, O'Brien P, Otway DJ, White AJP, Williams DJ, Jones AC. Studies on mixed β-diketonate/isopropoxide compounds of zirconium and hafnium, the X-ray single-crystal structures of $[M_2(OPr^i)_6(tmhd)_2]$ (M = Zr, Hf): some chemistry important in the MOCVD of oxides. Inorg Chem 1999;38(7):1432–7. https://doi.org/10.1021/ic980690w.
[53] Hwang SM, Lee SM, Park K, Lee MS, Joo J, Lim JH, et al. Effect of annealing temperature on microstructural evolution and electrical properties of sol-gel processed ZrO_2/Si films. Appl Phys Lett 2011;98(2):22903. https://doi.org/10.1063/1.3541784.
[54] Moulder JF, Chastain J. Handbook of x-ray photoelectron spectroscopy: a reference book of standard spectra for identification and interpretation of XPS data. Eden Prairie, Minn. Physical Electronics Division, Perkin-Elmer Corp; 1992.
[55] Juan P, Liu C, Lin C, Ju S, Chen M, Chang IY, et al. Electrical characterization and dielectric properties of metal–oxide–semiconductor structures using high-κ $CeZrO_4$ ternary oxide as gate dielectric. Jpn J Appl Phys 2009;48(5):05DA02. https://doi.org/10.1143/JJAP.48.05DA02.
[56] Morant C, Sanz JM, Galan L. Ar-ion bombardment effects on ZrO_2 surfaces. Phys Rev B 1992;45(3):1391–8. https://doi.org/10.1103/PhysRevB.45.1391.
[57] Biira S, Thabethe TT, Hlatshwayo TT, Bissett H, Ntsoane T, Malherbe JB. Investigating the thermal stability of the chemical vapour deposited zirconium carbide layers. J Alloys Compd 2020;834:155003. https://doi.org/10.1016/j.jallcom.2020.155003.
[58] Hakiki NE, Montemor MF, Ferreira M, Da Cunha Belo M. Semiconducting properties of thermally grown oxide films on AISI 304 stainless steel. Corrosion Sci 2000;42(4):687–702. https://doi.org/10.1016/S0010-938X(99)00082-7.
[59] Sabioni ACS, Ramos RPB, Ji V, Jomard F, Macedo WAdA, Gastelois PL, et al. About the role of chromium and oxygen ion diffusion on the growth mechanism of oxidation films of the AISI 304 austenitic stainless steel. Oxid Met 2012;78(3–4):211–20. https://doi.org/10.1007/s11085-012-9301-y.
[60] Garvie RC, Goss MF. Intrinsic size dependence of the phase transformation temperature in zirconia microcrystals. J Mater Sci 1986;21(4):1253–7. https://doi.org/10.1007/BF00553259.
[61] Vainshtein BK. Structure analysis by electron diffraction. Burlington: Elsevier Science; 1964.
[62] Fedel M, Franch J, Rossi S. Effect of thickness and sealing treatments on the corrosion protection properties of anodic oxide coatings on AA5005. Surf Coating Technol 2021;408:126761. https://doi.org/10.1016/j.surfcoat.2020.126761.
[63] Li J, Ecco L, Fedel M, Ermini V, Delmas G, Pan J. In-situ AFM and EIS study of a solventborne alkyd coating with nanoclay for corrosion protection of carbon steel. Prog Org Coating 2015;87:179–88. https://doi.org/10.1016/j.porgcoat.2015.06.003.
[64] Ngo NK, Shao S, Conrad H, Sanders SF, D'Souza F, Golden TD. Synthesis, characterization, and the effects of organo-grafted nanoparticles in nickel coatings for enhanced corrosion protection. Mater Today Commun 2020;25:101628. https://doi.org/10.1016/j.mtcomm.2020.101628.
[65] Cabrini M, Cigada A, Rondell G, Vicentini B. Effect of different surface finishing and of hydroxyapatite coatings on passive and corrosion current of Ti_6Al_4V alloy in simulated physiological solution. Biomaterials 1997;18(11):783–7. https://doi.org/10.1016/S0142-9612(96)00205-0.
[66] Zhao Qi, Zhang Li. Electrochemical impedance spectroscopy investigation on the corrosive behaviour of waterborne silicate micaceous iron oxide coatings in seawater. Coatings 2019;9(7):415. https://doi.org/10.3390/coatings9070415.
[67] Bierwagen GP, He L, Li J, Ellingson L, Tallman D. Studies of a new accelerated evaluation method for coating corrosion resistance — thermal cycling testing. Prog Org Coating 2000;39(1):67–78. https://doi.org/10.1016/S0300-9440(00)00106-5.
[68] Yao Z, Xu Y, Liu Y, Wang D, Jiang Z, Wang F. Structure and corrosion resistance of ZrO_2 ceramic coatings on AZ91D Mg alloys by plasma electrolytic oxidation. J Alloys Compd 2011;509(33):8469–74. https://doi.org/10.1016/j.jallcom.2011.06.011.
[69] Meráz JS, Fernández F, Magaña LF. A method for the measurement of the resistance of electrolytic solutions. J Electrochem Soc 2005;152(4):E135. https://doi.org/10.1149/1.1867612.
[70] Zoltowski P. On the electrical capacitance of interfaces exhibiting constant phase element behaviour. J Electroanal Chem 1998;443(1):149–54. https://doi.org/10.1016/S0022-0728(97)00490-7.
[71] Zhang FD, Liu H, Suebka C, Liu YX, Liu Z, Guo W, et al. Corrosion behaviour of laser-cleaned AA7024 aluminium alloy. Appl Surf Sci 2018;435:452–61. https://doi.org/10.1016/j.apsusc.2017.11.141.
[72] Hinderliter BR, Croll SG, Tallman DE, Su Q, Bierwagen GP. Interpretation of EIS data from accelerated exposure of coated metals based on modeling of coating physical properties. Electrochim Acta 2006;51(21):4505–15. https://doi.org/10.1016/j.electacta.2005.12.047.
[73] Stafford OA, Hinderliter BR, Croll SG. Electrochemical impedance spectroscopy response of water uptake in organic coatings by finite element methods. Electrochim Acta 2006;52(3):1339–48. https://doi.org/10.1016/j.electacta.2006.07.047.

[74] Amand S, Musiani M, Orazem ME, Pébère N, Tribollet B, Vivier V. Constant-phase-element behavior caused by inhomogeneous water uptake in anti-corrosion coatings. Electrochim Acta 2013;87:693–700. https://doi.org/10.1016/j.electacta.2012.09.061.

[75] Liu GX, Liu A, Meng Y, Shan FK, Shin BC, Lee WJ, et al. Annealing dependence of solution-processed ultra-thin ZrO_x films for gate dielectric applications. J Nanosci Nanotechnol 2015;15(3):2185–91. https://doi.org/10.1166/jnn.2015.10228.

[76] Zuo Y, Pang R, Li W, Xiong JP, Tang YM. The evaluation of coating performance by the variations of phase angles in middle and high frequency domains of EIS. Corrosion Sci 2008;50(12):3322–8. https://doi.org/10.1016/j.corsci.2008.08.049.